5.6   TWO-COMPONENT HORIZONTAL MOTION VECTORS FROM SCANNING
EYE-SAFE AEROSOL LIDAR AND CROSS-CORRELATION

Shane D. Mayor*

Department of Physics, California State University Chico

Abstract

Two-component horizontal motion vectors are de-
rived through the cross-correlation of aerosol features
in sequences of near-horizontal scans collected by
the Raman-shifted Eye-safe Aerosol Lidar (REAL) at
the 2007 Canopy Horizontal Array Turbulence Study
(CHATS). Time-series comparisons of the velocity com-
ponents representative of square regions surrounding an
instrumented tower are compared with averaged sonic
anemometer data. Results from the current implemen-
tation of the algorithm show that more than 80% of
47,000 u-components from 10 s scan update periods and
500 m $\times$ 500 m blocks are within $\pm$ 1 m s^{-1} of the
corresponding time-averaged anemometer data. In gen-
eral, better agreement is found at night when the atmo-
sphere has lower turbulent kinetic energy (TKE). During
the day, when the atmosphere is unstable and turbulent,
the agreement becomes poorer—presumably the result
of a less uniform velocity field and the two very differ-
ent sampling and measurement methods. Distributions
of the velocity differences are shown as a function of
hour, TKE, strength of the peak of the cross-correlation
function (CCF), and signal-to-noise ratio (SNR) of the
raw backscatter data. It is shown that larger block ar-
eas, shorter time between scans, lower TKE, higher
CCF maximas, and stronger SNR contribute to improved
agreement. The results also reveal that the u-components
are in better agreement than the v-components. A reason
for this discrepancy is not known at the time of this writ-
ing.

1.   INTRODUCTION

Remote measurements of the vector wind field in the
atmospheric boundary layer from ground-based loca-
tions on the order of kilometers away from the area of
interest are still needed in several applications. Examples
include wind resource assessments and monitoring near
established wind farms; determining the initial transport
and dispersion of hazardous materials (i.e. nuclear power

and industrial chemical sites); wind shear and wake vor-
tex detection near airports; and micro-meteorological re-
search. Doppler lidars provide precise direct measure-
ments of only the radial component of motion. However,
in many of the above applications it is not practical to
collect 360° azimuth scans or assume horizontal homo-
geneity of the atmospheric boundary layer, or combine
radial measurements with numerical flow retrieval mod-
els, to derive two or more wind components from a single
Doppler lidar. The use of two Doppler lidars separated
by several kilometers can provide multiple wind com-
ponents over a common area, but this is likely to be a
prohibitively expensive solution in many cases. Instead,
a direct observation of two or more components of the
vector wind field is desired from scanning over a sector
with a single instrument. It is in this scenario that the
application of the cross-correlation technique to aerosol
backscatter lidar images may hold significant value.

The cross-correlation technique has been applied to
aerosol lidar data several times previously (Eloranta
et al., 1975; Sroga et al., 1980; Kunkel et al., 1980;
Sasano et al., 1982; Hooper and Eloranta, 1986; Kolev
et al., 1988; Schols and Eloranta, 1992; Piironen and
Eloranta, 1995; Mayor and Eloranta, 2001). Similar ap-
proaches were also applied to weather radar data (Rine-
hart and Garvey, 1978) and satellite images (Leese et al.,
1971). The most recent of these papers (Mayor and
Eloranta, 2001) showed two-component vector fields
with 250 m horizontal resolution over areas as large
as 60 km^2. These vectors however were the result of
large amounts of temporal averaging of many cross-
correlation functions—up to 41 minutes in one case. Fur-
thermore, the lidar system used in Mayor and Eloranta
(2001) was not eye-safe and the scans were not coinci-
dent with any independent forms of wind measurement
for validation.

In the present work, no temporal averaging of the
cross-correlation functions was performed. The data was
collected with an eye-safe elastic lidar operating at 1.5-
microns wavelength (Mayor et al., 2007) and an instru-
mented tower penetrated the lidar scan plane. The re-
mote and in situ data were collected nearly continuously
over three months. The data set enables a comprehensive
evaluation of the technique.

Corresponding author address: Shane D. Mayor, Department of
Physics, California State University Chico, Chico, CA 95929; *e-mail*:
sdmayor@csuchico.edu

2. EXPERIMENT

The data used in this study were collected between 14 March and 11 June 2007 in Dixon, California, during the Canopy Horizontal Array Turbulence Study (CHATS) (Patton et al., 2011). The REAL was located 1.61 km directly north of the NCAR Integrated Surface Flux Facility (ISFF) 30-m vertical tower (VT) (see Fig. 1). The VT was located in a large orchard of 10 m tall walnut trees. The VT supported 13 Campbell Scientific CSAT3 3-D sonic anemometers of which 5 were located above the tree tops at 12.5, 14, 18, 23, and 29 m above ground level (AGL). The flat terrain in the vicinity of the experiment, relatively short height and uniformity of the orchard, and absence of additional obstructions between the lidar and the orchard enabled nearly horizontal scans to be collected over a wide area surrounding the orchard. The lidar's laser beam, which was projected from the REAL at a height of 4.2 m AGL, passed just above the tops of the trees in the orchard and intersected the VT at a height of approximately 12.5 m AGL. The approximate elevation angle during the vast majority of PPI scans was $0.2°$. Assuming the terrain is perfectly flat, this corresponds to a slope of 3.5 m per kilometer. Therefore, the PPI scans were well within the roughness sublayer and the derived motion vectors are essentially horizontal. The laser beam at the point where it is emitted from the lidar is 6.6 cm in diameter and has a half-angle divergence of 0.12 mrad. This results in a beam diameter of 45 cm at 1.61 km range and 1 m at 4 km range. The laser pulse duration was 6 ns which corresponds to 1.8 m length.

The REAL operated at CHATS with a constant pulse repetition frequency (PRF) of 10 Hz. However, all other parameters controlling the scans were variables that could be altered in order to optimize the scans to achieve a variety of experimental objectives, some that were weather dependent. The variables include the angular scan rate, the angular range of a scan, and the sequence of scan types to be performed. In summary, a large number (approximately 200,000) of the PPI scans collected were intended to reveal a broader view of the experimental area. These are called "wide" and ranged from approximately $150°$ to $210°$ azimuth and were performed at a rate of $4° \text{ s}^{-1}$. Another large percentage of the PPI scans (approximately 75,000) were termed "narrow" and were intended to probe the fine-scale structure and motion of the atmosphere in the immediate vicinity of the tower. The narrow scans ranged from $175°$ to $185°$ azimuth.

At an azimuthal scan rate of $4° \text{ s}^{-1}$, and a PRF of 10 Hz, the distance between laser pulses in the east-west direction at the range of the VT was 11 m. The backscatter signal digitization rate was 100 million samples per second corresponding to a point every 1.5 m in range. As a

Figure 1: Diagram of the experimental area. The shaded regions from $150°$ – $210°$ and $175°$ – $185°$ azimuth represent the areas covered by "wide" and "narrow" PPI scans, respectively. The tower was located 1.61 km directly south of the lidar. The squares centered on the tower represent the regions extracted from the gridded scan data that were used to compute motion vectors via the cross-correlation technique.

result of this pulse rate, scan speed, and digitization rate, the number of data points in the native spherical coordinate system of the lidar falling into blocks that are 250 m × 250 m, 500 m × 500 m, 750 m × 750 m, and 1 km × 1 km, and centered on the VT are 3692, 14885, 33650, and 60222, respectively. After interpolation to a Cartesian grid with spacing of 10 m in both east-west and north-south dimensions, the number of points in the blocks are 625, 2500, 5625, and 10000, respectively.

The VT intersected the 0.2 degree elevation PPI scan surface at about 12.5 m AGL (see Fig. 2). However, a hard target reflection from the tower does not always appear in the PPI images. This is because the beams were separated by approximately 11 m at the range of the tower during a $4° \text{ s}^{-1}$ scan. The laser beam steering unit operated independently of the 10 Hz transmitter and, as a result, laser pulses were usually not projected at the same azimuth angles from one scan to the next. The central column of the tower was 32 cm wide. Guy wires 0.47 cm in diameter were attached to the tower at 4 heights on the tower. Guy wires from 7.9 and 18.8 m AGL were anchored into the ground 13.4 m from the tower base. Guy wires 23.8 and 32.0 m AGL were anchored into the ground 26.8 m from the base.
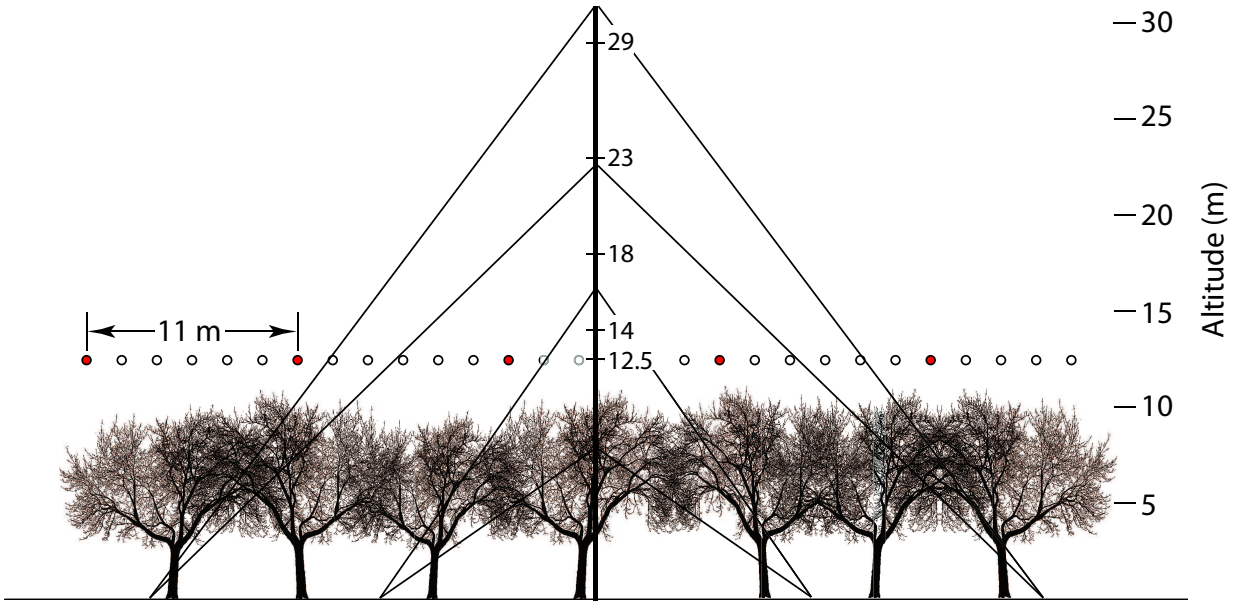
Figure 2: Diagram showing the altitude, spacing, and size of REAL laser pulses with respect to the tree tops and the vertical tower at CHATS. This diagram is an east-west cross section looking either towards or away from the lidar. Laser pulses colored red are from the same scan at an azimuthal scan rate of 4° s^{-1} and spaced 11 m apart at this range of 1.61 km from the lidar.

3. ALGORITHM

A program has been developed in Interactive Data Language (IDL) to calculate the motion vectors using the aerosol backscatter data and the cross-correlation technique. As a first step, the raw lidar returns, in their native spherical coordinate system, are processed on a shot by shot basis by calculating and subtracting the mean background from each waveform; multiplying the waveform by the square of the range to remove the one-over-range-squared dependence of the raw signal and converting to decibels. Each return is low-pass and high-pass median filtered to remove single point outliers and large scale features such as the effects of attenuation and the inability to normalize for shot-to-shot laser pulse energy variations, respectively. For the results shown here, the low-pass filter length was set to 7 points corresponding to 10.5 m and the high-pass filter length was set to 333 points corresponding to 500 m.

After processing the returns from a scan as described above, the data are interpolated to a Cartesian grid with 10 m grid-point spacing in both east-west and north-south directions. This step is implemented by use of the IDL polar_surface.pro function. In addition to the processed backscatter data, time and signal-to-noise ratio (SNR) data are interpolated to Cartesian arrays so that this information can easily be extracted over the exact block regions that the correlation technique will be applied to. A temporal median is computed for all points on the Cartesian grid. This is based on all of the PPI scans contained in each raw data file that currently span approximately 1 hour of time. A single raw data file typically contains dozens to hundreds of scans.

Next, subsets of the gridded data are extracted in square regions corresponding to the 4 blocks shown in Fig. 1. For this work, vectors were calculated from 250 m × 250 m, 500 m × 500 m, 750 m × 750 m, and 1 km × 1 km blocks to investigate the effect of block size. Blocks of the same size and position and from pairs of consecutive scans are used to calculate each motion vector. Histogram equalization is applied to each block (Schols and Eloranta, 1992). Two-dimensional cross-correlation functions (CCF) are computed using fast-Fourier transforms and the Wiener-Khinchin theorem. The 9 × 9 points centered on the peak of the CCF are used to calculate a bicubic natural nonsmoothing spline with 100 × 100 point resolution. The location of the peak of this numerically fit function corresponds to the displacement caused by the predominant motion within the block area over two scans. The velocity is determined by dividing the displacement by the time between scans. In addition to the above, average lidar SNR and the average image SNR of the block regions is computed for data analysis.

The current version of the program to calculate wind
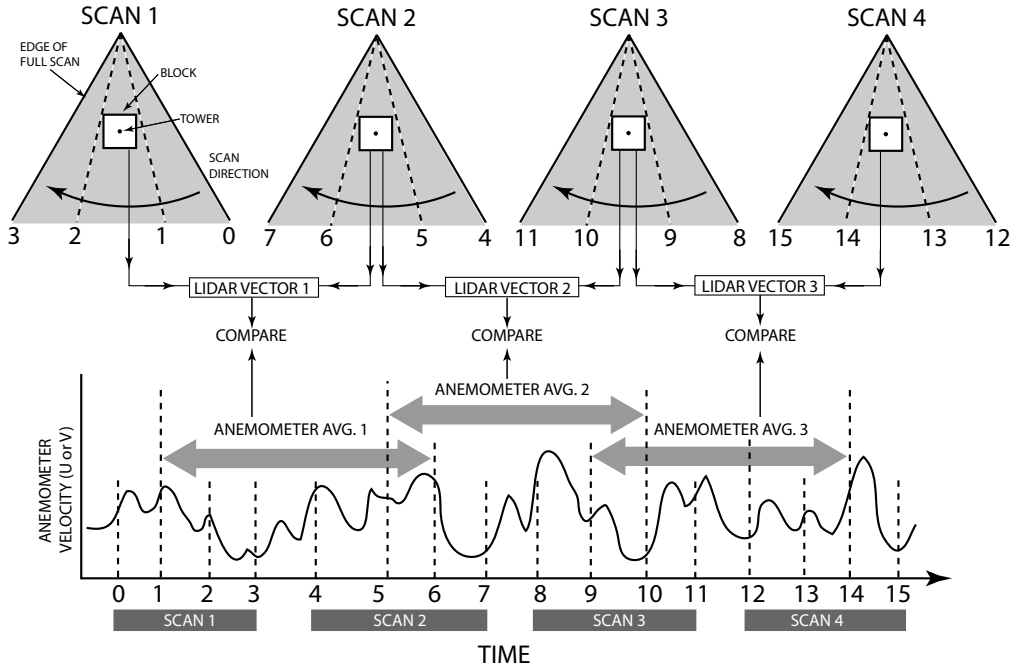
Figure 3: Visual depiction of how anemometer time series data was averaged for comparison with the vectors derived from lidar scans. This example considers a series of four consecutive PPI scans that result in three vectors. The anemometer data are averaged over the periods corresponding to when the lidar's beam enters the block on the first scan (positions 1, 5, and 9 in time) and exits the block on the subsequent scan (positions 6, 10 and 14 in time).

vectors from the lidar data neglected to incorporate improvements described by Piironen and Eloranta (1995). Specifically, they show that fitting a Gaussian to the peak of the CCF results in less random error than the bicubic natural spline that was described by Schols and Eloranta (1992). We are presently replacing the bicubic spline with the Gaussian method and expect to have improved results later this year.

4. DATA PROCESSING

The primary objective of this research is to determine the accuracy and reliability of the cross-correlation method for remote determination of the 2-component wind vector. Therefore, a reference wind measurement is needed for comparison and the sonic anemometer data from the VT at 12.5 m AGL provide this. However, the sonic anemometer data are at 60 Hz and the nature of the lidar and the sonic anemometer measurements are very different. The lidar vectors are based on the drift of macroscopic aerosol features over relatively large areas. The sonic anemometer data are based on air motion at essentially a point. The anemometer measurement is performed 60 times per second while the cross-correlation technique currently results in a measurement once every

10 to 30 s. Therefore, substantial time averaging of the sonic anemometer data is required to make a comparison with each lidar vector. Presently, we arbitrarily chose to average the anemometer data over the time required for the lidar to sweep across the block twice (see Fig. 3). This choice may or may not be optimal. Further research is required to determine optimal averaging of the sonic anemometer data.

Agreement between the two forms of measurements is likely to vary in space and time and depend on several factors such as the presence of aerosol features in the block and the amount of noise in the data. Therefore, a secondary objective is to identify other variables that can be extracted from the lidar data and are related to the agreement between the motion vectors and the anemometer data. Doing so is expected to enable the development of a method to estimate the likelihood that a derived vector is representative of what an anemometer would measure in the region. Knowing this would provide the ability to disregard noisy vectors in two-dimensional flow fields. A third objective is to elucidate the dynamic atmospheric processes that may influence agreement of the two forms of wind measurements. To gain insight on possible processes, turbulent kinetic energy (TKE) and gradient Richardson number (GRN)

have been calculated from the in situ data. Therefore, for each vector computed, the program also calculates and records the maximum of the CCF, the mean SNR of the raw lidar data in both blocks, the mean SNR of the images in the two blocks, the TKE, and the GRN. Results of GRN are not presented in this paper.

5. Results

The author's original hypothesis of this research was that the correlation method would perform best during the daytime when the surface layer tended to be either neutral or unstable thereby promoting mixing and aerosol inhomogeneities that advect with the mean horizontal wind. A corollary hypothesis was that the correlation method would fail at night when the surface layer tends to become stable, the aerosol distribution more stratified, and gravity waves are supported. Because gravity waves are observed in the aerosol imagery, and wave propagation may not equal the local wind speed and direction, it was thought that waves would prevent the method from performing well at night—especially under weak wind conditions.

Results shown here demonstrate that the opposite is true: the best agreement between the lidar-derived wind components and averaged sonic anemometer data tends to occur at night when the TKE is low. This can be seen in time-series comparisons (Figs. 4 and 5) and in statistical results (Figs. 6 through 11). It is also shown here that the performance of the cross-correlation method is related to the amplitude of the peak of the CCF (Figs. 12 and 13) and the SNR of the raw backscatter data (Figs. 14 and 15). This section is concluded with Fig. 16 that summarizes the agreement as a function of both block size and time between scans. For the results shown in Figs. 6 through 15, only vectors that resulted from 500 m × 500 m blocks with 17 s scan update times, and corresponding averaged sonic anemometer data, were chosen. This enabled a sample size of approximately 100,000 vector comparisons.

5.1 21 March 2007: Weakly stable evening case

Fig. 4 shows time-series comparisons from the evening of 21 March 2007 between 04:15 and 06:45 UTC. This 2.5 hour period occurred during the evening from about sunset until 15 minutes before midnight when the atmospheric surface layer was weakly stable (z/L stability parameter at 12.5 m AGL was +0.035) and the winds were light (less than 2 m s^{-1} for the most part) and variable. The lidar was programmed to repeat a sequence of 40 consecutive PPI scans followed by 2 consecutive RHI scans. The PPI scans ranged from 150° to 210° azimuth at a scan rate of 4° s^{-1}. This resulted in one scan

every 17.3 s. For the results shown in Fig. 4, motion vectors were calculated from pairs of 250 × 250 m blocks. The top panel shows the u-components (east-west components) and the bottom panel shows the v-components (north-south components). Black points are from the lidar and red points are from the averaged 12.5 m AGL sonic anemometer data. Time-lapse animations of the lidar backscatter images from this case show what appear to be a substantial amount of gravity wave activity and episodes of turbulence during this period.

5.2 26 April 2007: Unstable afternoon case

Fig. 5 shows time-series comparisons from the afternoon of 26 April 2007 between 22:00 UTC on 26 April and 01:00 UTC on 27 April 2007. The lidar was programmed to collect alternating RHI and PPI scans. This resulted in one PPI scan (or one RHI scan) every 30 s. The PPI scans were directed between 151° and 211° azimuth at a scan rate of 4° s^{-1}. During this period, a density current front passed over the experimental site at 23:25 UTC on 26 April (see Mayor (2011) for more information). The z/L stability parameter at 12.5 m height ranged from –2.0 to –0.6 (strongly to moderately unstable) before the arrival of the front to –0.5 to –0.2 (moderately to weakly unstable) after the passage of the front. During the entire period, wind speeds remained below approximately 4 m s^{-1}. However, the wind direction changed dramatically from 350° (N) before the front to 221° (SSW) after the front. These results show a lack of correlation between the two forms of wind measurement on the shortest time intervals. However, the abrupt near-reversal of the v-component in both time-series demonstrates that the mean flow is captured. The difference between this case and the former is attributed to the more turbulent conditions of this case. In the next section, it is shown how increased TKE results in less agreement between the two measurements.

5.3 Statistical results

5.3.1 Agreement as a function of hour of day

To clarify whether the cross-correlation technique results in better agreement during the day or night, the differences with anemometer data were binned according to the hour of the day in which they occurred and 0.1 m s^{-1} velocity-difference increments. Figs. 6 and 7 show these distributions. The $U_{lidar} - \overline{U}_{sonic}$ distributions all show maxima in either the 0.0 or 0.1 m s^{-1} bins. The $V_{lidar} - \overline{V}_{sonic}$ distributions show maxima ranging from –0.1 to 0.2 m s^{-1}. The blue colored distributions are from hours during the night. The violet colored distributions are from hours during the day. These results show
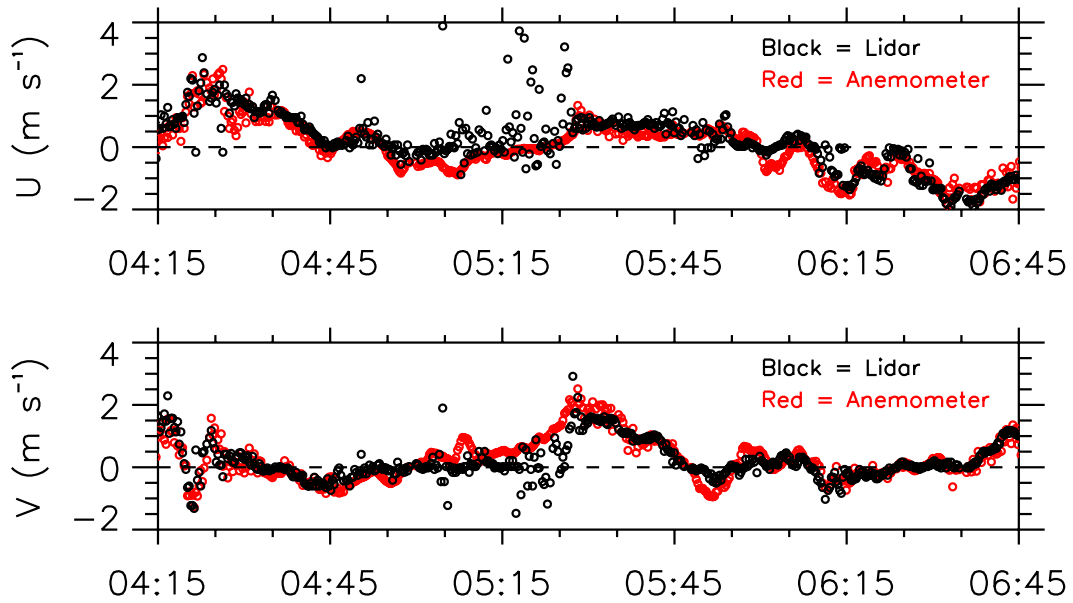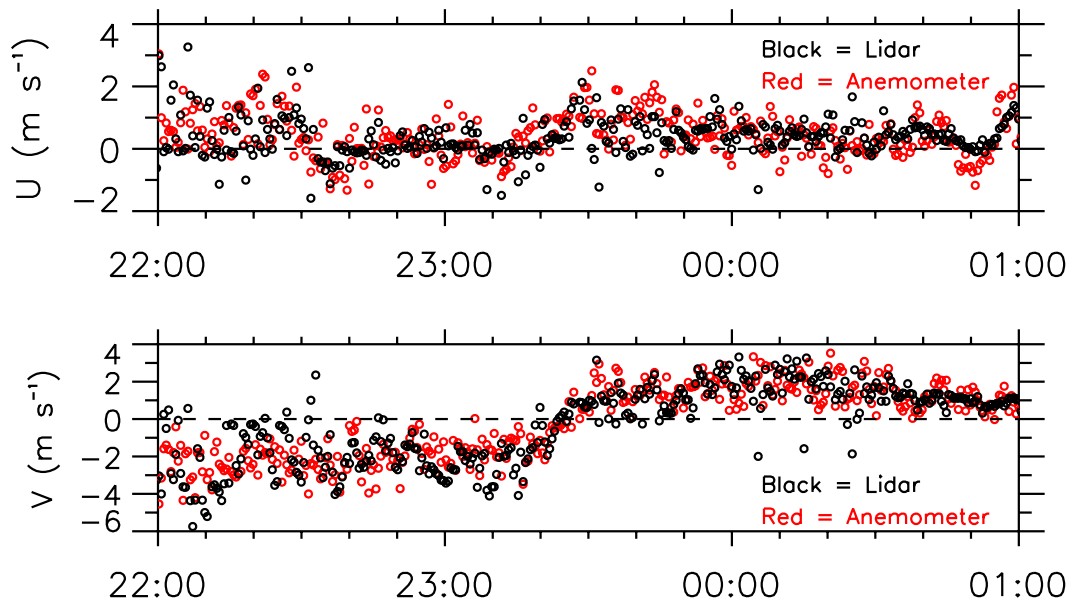
Figure 4: Comparison of u-component (top) and v-component (bottom) from sonic anemometer data (red points) and the cross-correlation technique applied to the lidar data (black points) over a 2.5-hour time span on the evening of 21 March 2007. During this period the atmosphere was weakly stable and the winds were light and variable. Lidar data points were calculated from 250 m × 250 m regions centered on the ISFF tower from pairs of frames at 17.3 s intervals.

Figure 5: Comparison of u-component (top) and v-component (bottom) from sonic anemometer data (red points) and the cross-correlation technique applied to the lidar data (black points) over a 3-hour time span on the afternoon of 26–27 April 2007. During the middle of this period, a density current front passed over the experimental site approximately reversing the wind direction from south to north (the v-component). Due to the collection of alternating PPI and RHI scans, the PPI frames used to calculate the motion were spaced in time at 30 s intervals. The algorithm used a 500 m × 500 m block centered around the tower supporting the sonic anemometer.

that the agreement between the lidar-derived and averaged anemometer wind components is indeed better during the night as the distributions from those hours are narrower.

5.3.2 Agreement as a function of TKE

To explore the relationship between the agreements as a function of turbulent kinetic energy (TKE), the differences were binned into TKE increments of 0.25 m² s⁻² and differences of 0.1 m s⁻¹. The resulting distributions are shown in Figs. 8 and 9. The narrowest distribution (blue) corresponds to the lowest TKEs ($0 - 0.25$ m² s⁻²) while the broadest distribution (violet) correspond to the highest TKEs ($2.25 - 2.50$ m² s⁻²). Next, to confirm that TKE tends to be low at night and high during the day, distributions of TKE were binned into 0.25 m² s⁻² and 1-hour time intervals and shown in Figs. 10 and 11. These results confirm that TKE does tend to be increased during the day (broader distributions) and reduced (narrower distribution) at night. Together, these findings support a new hypothesis that the agreement between lidar-derived wind components and averaged sonic anemometer wind components is mostly related to the degree of uniformity of the velocity field. During the night, static stability suppresses turbulence resulting in a more uniform velocity field.

5.3.3 Agreement as a function of CCF maximum

Figs. 12 and 13 in this paper show how the agreement between lidar-derived motion components and averaged sonic anemometer data varies as a function of the maximum of the CCF. Clearly, the distributions narrow as the CCF maximum increases. Note that of the 9 curves plotted, the one corresponding to the 0.1 to 0.2 range contains the most samples. Therefore, in the future, substantial improvement to the velocity measurement capability during a field campaign could be realized by simply programming the lidar to avoid long periods between PPI scans.

Why should the amplitude of the CCF peak be related to the agreement of the two forms of measurements? Fig. 22 of Mayor et al. (2003) shows how the peak of the cross-correlation function decreases as the time between scans increase. The decrease is due to the deformation of aerosol features by small-scale turbulence. (If the features did not change shape over time, the peak of the CCF would remain constant at 1.) One possible reason is that by changing shape, there is increased possibility that the maximum of the cross-correlation will not occur precisely at the location of displacement due to the mean wind but instead a nearby location on the CCF.

5.3.4 Agreement as a function of SNR

Raw SNR is computed by dividing each element of the background-subtracted backscatter waveform by the standard deviation of a set of points that was collected immediately prior to the laser discharge. (See section 3.1 and Fig. 6b in Mayor (2008) for more on this topic.) It is termed "raw SNR" to distinguish it from "image SNR". The raw SNR data are gridded so that averages over the exact block regions can be obtained. The raw SNR is dependent upon the performance of the specific lidar system and the local atmospheric conditions.

Figs. 14 and 15 show how the agreement varies as a function of mean raw SNR from the backscatter data in the two blocks used to compute the CCF. The plots suggest significant improvement as SNR increases, especially up to about 150. The distributions do not appear to narrow significantly above that.

6. Summary

In general, gravity wave propagation does not appear to present a significant problem for deriving wind vectors from the cross-correlation technique during stable conditions. However, case studies are required to confirm this by examining time-series comparisons when wave packets were passing through the tower site. Contrary to the author's original hypothesis, results show that the lidar-derived wind components are in better agreement with the averaged sonic anemometer wind components during the night when the gravity waves may be present. Results show that the agreement is strongly a function of TKE. Results also show that large CCF maxima and increased raw SNR tend to support improved agreement.

Fig. 16 summarizes the agreement of the vector components for various block sizes and time between scans. The height of the bars indicate the percentage of observations falling within $\pm$ 1 m s⁻¹ and $\pm$ 2 m s⁻¹ of each other. The best agreement (tallest bars) were achieved with small scan update periods and large blocks. This result is consistent with the idea that large blocks are more likely to capture a larger number of aerosol features (spatial perturbations in the aerosol backscatter field) and that quick update times enable capturing the aerosol features in the second scan before they have changed shape substantially. Fig. 16 also shows the agreement of the v-components to be systematically slightly less than the u-components. The cause of this is not known at the time of this writing. It may be a flaw in the algorithm or a bug in the code.

It is important to keep in mind that the lidar-derived vectors are not the average of the velocity distribution over the block area or the period of time spanning the two scans. Instead, they are the result of observing the ini-
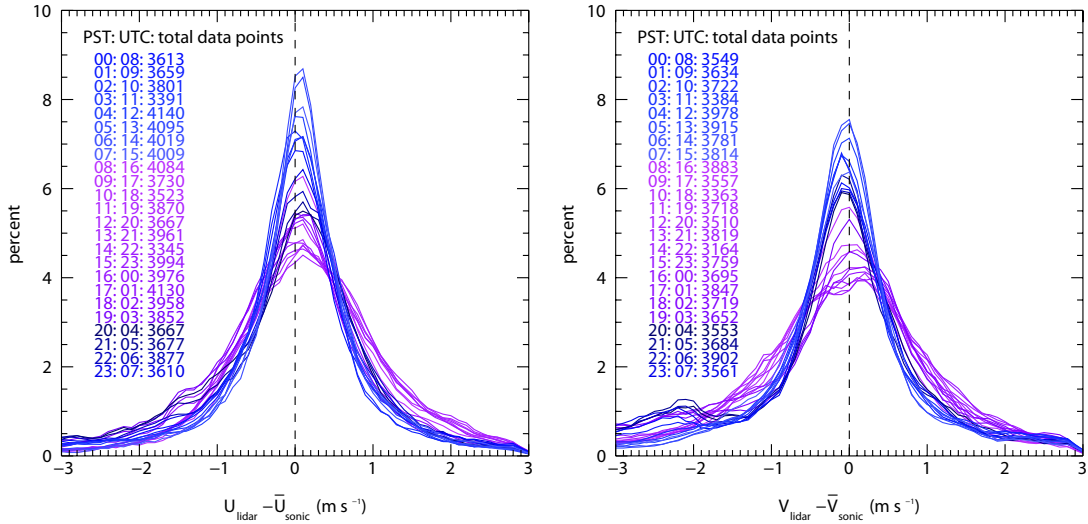
Figure 6: Distributions of the velocity component differences. Left panel: u-component differences ($U_{lidar} - \overline{U}_{sonic}$). Right panel: v-component differences ($V_{lidar} - \overline{V}_{sonic}$). The lidar-derived components resulted from 500 m × 500 m blocks and 17 s time between scans. Velocity differences were binned into 1-hour intervals in time and 0.1 m s^{-1} in velocity differences. A 3-point smooth was applied to each curve to reduce noise. The narrower blue curves are from the nighttime hours and the broader violet curves are from the daytime hours.
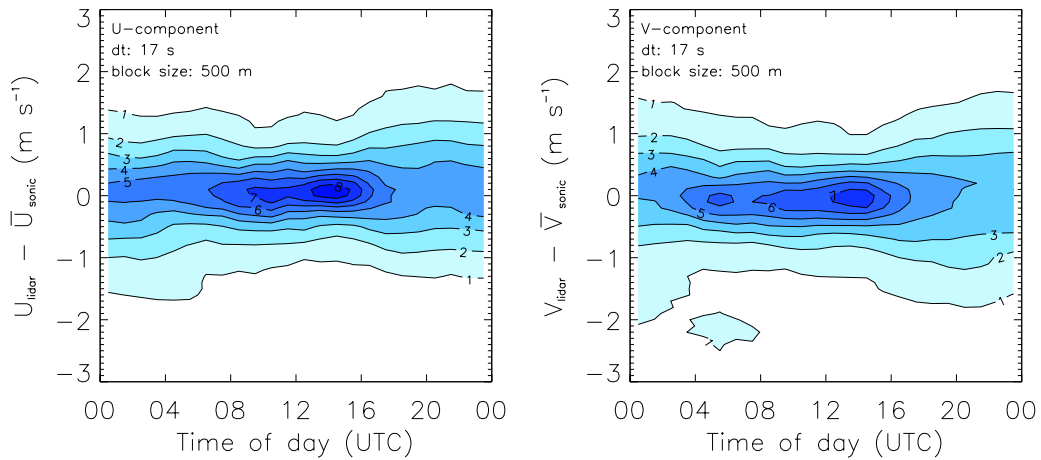
Figure 7: Same data as shown in Fig. 6 except as contour plots. Left panel: u-component differences ($U_{lidar} - \overline{U}_{sonic}$). Right panel: v-component differences ($V_{lidar} - \overline{V}_{sonic}$). Both as a function of time. The distributions narrow during the night indicating improved agreement during that time.
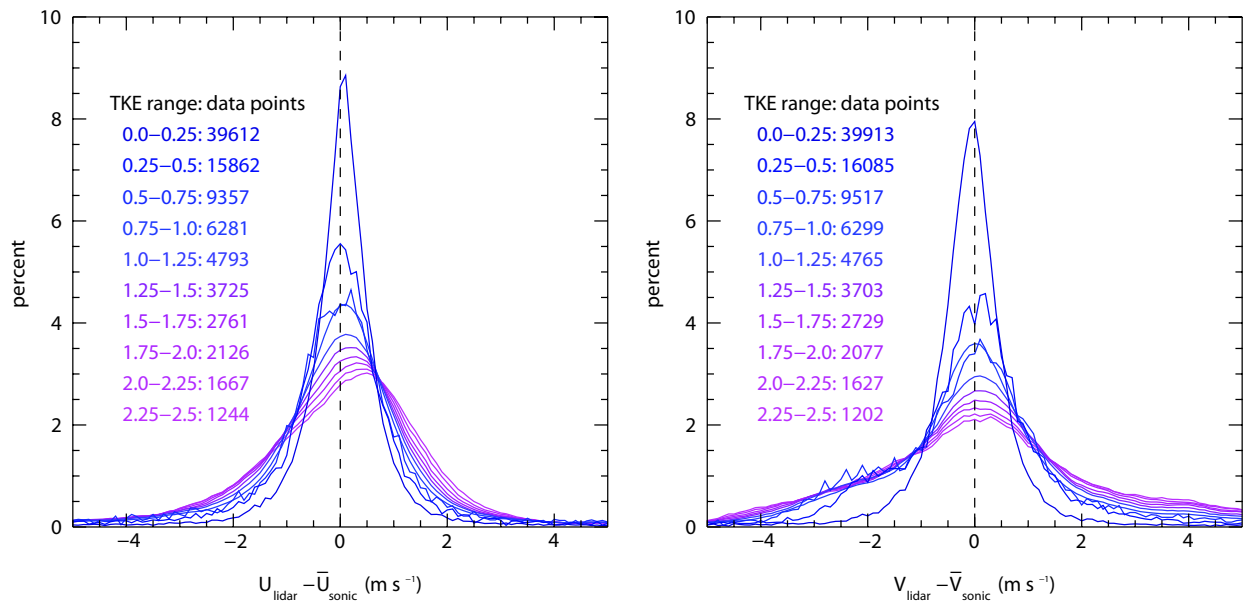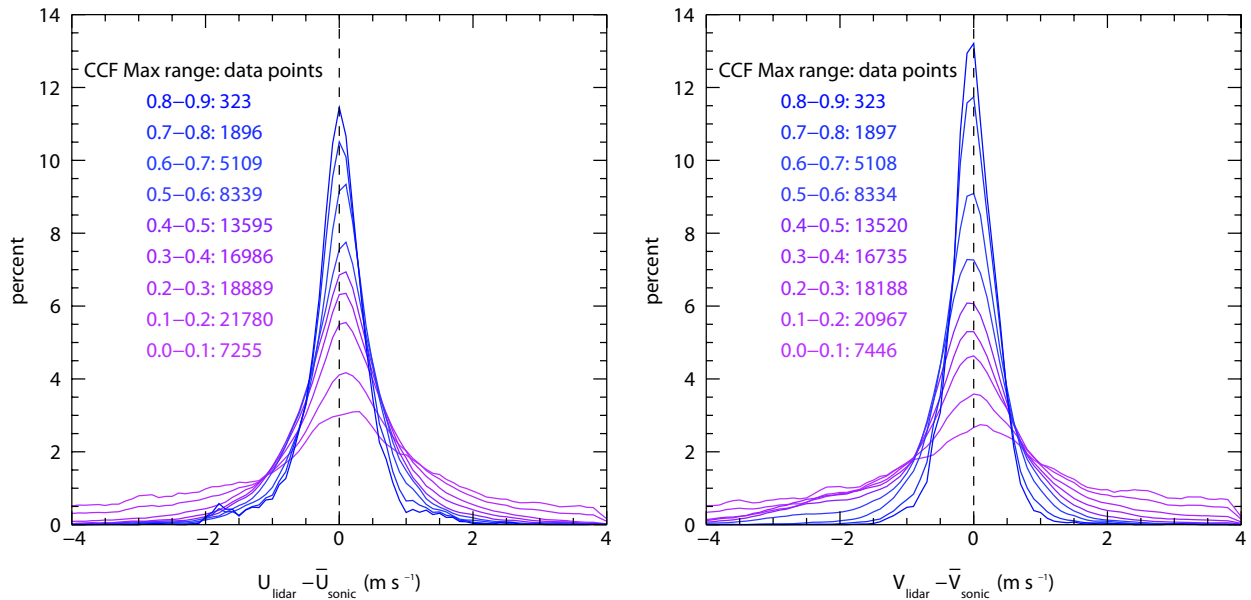
Figure 8: Distributions of the velocity component differences. In this case, each curve corresponds to a different range of turbulent kinetic energy (TKE) as measured by the sonic anemometer. The narrowest and tallest distribution (dark blue) occurs from the lowest range of TKEs ($0 - 0.25$ m^2 s^{-2}) while the shortest and broadest distribution (violet) occurs from the highest range of TKEs ($2.25 - 2.50$ m^2 s^{-2}). A 7-point smooth was applied to each curve to reduce noise. Note that the sample size of each distribution is printed on the figure and varies substantially.
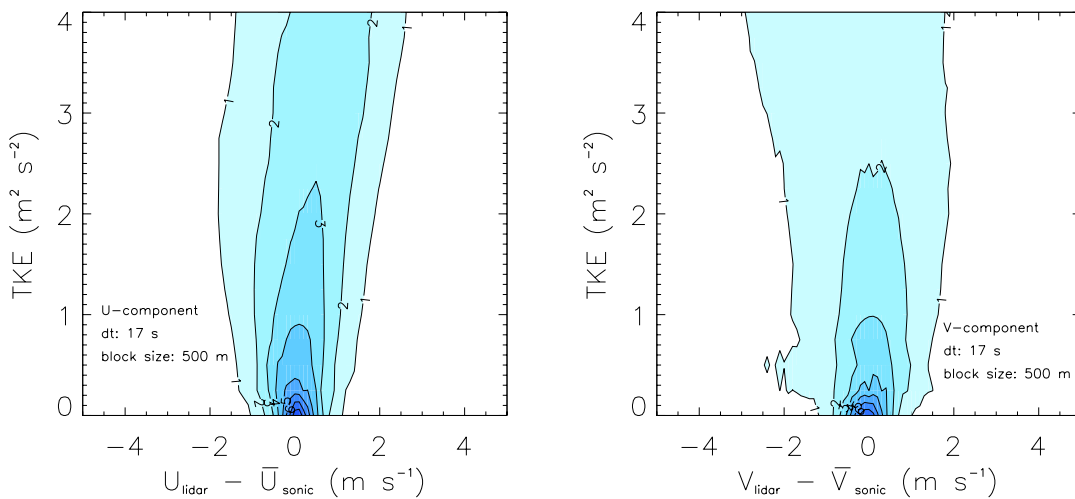
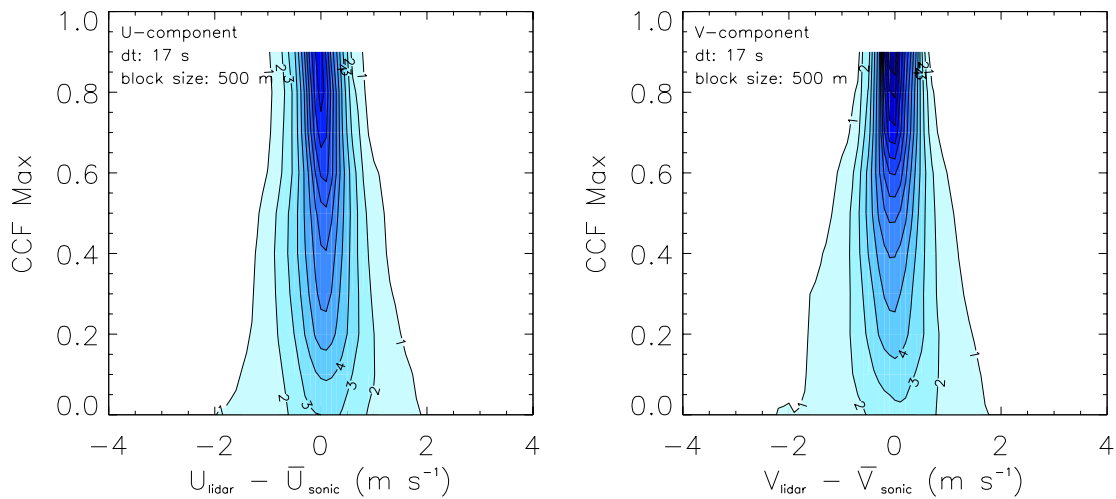

Figure 9: Same data as shown in Fig. 8 except as contour plots. Left panel: u-component differences ($U_{lidar} - \overline{U}_{sonic}$). Right panel: v-component differences ($V_{lidar} - \overline{V}_{sonic}$). Both as a function of TKE. The distributions broaden as TKE increases.
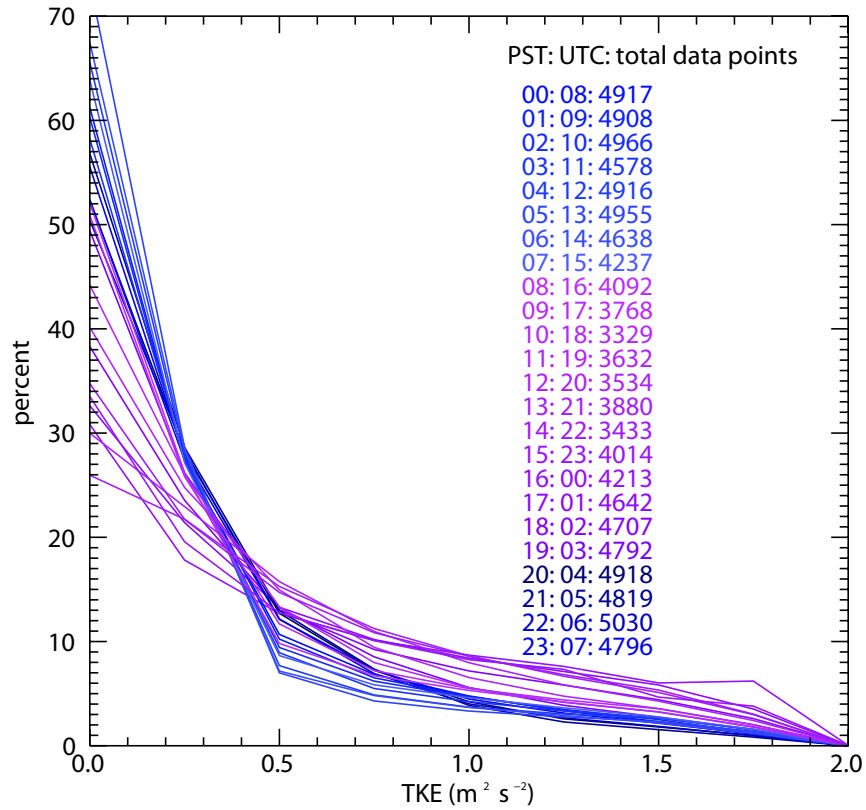
Figure 10: Distribution of turbulent kinetic energy (TKE) by hour. Violet curves occurred during the night. Violet curves occurred during the day.
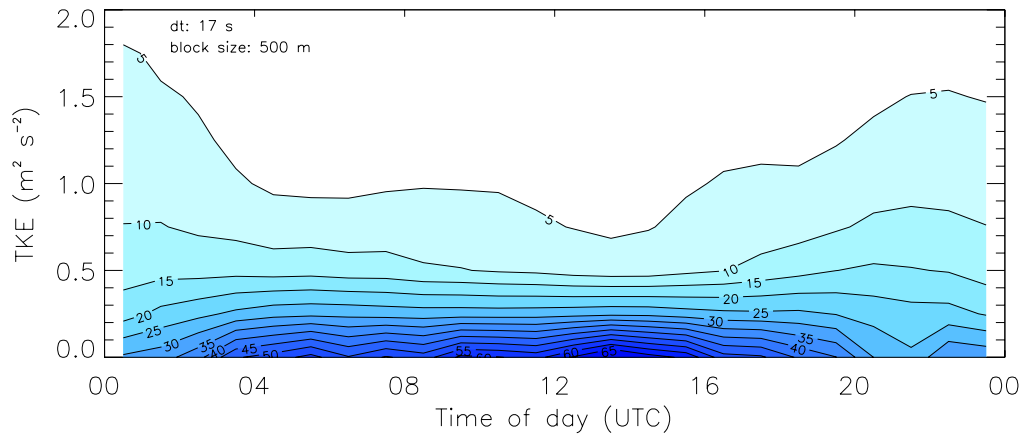
Figure 11: Same distributions of TKE as shown in Fig. 10, but shown as a contour plot.

Figure 12: Distributions of the velocity component differences as a function of the CCF maximum. In this case, each curve corresponds to a different range of CCF maximums. The narrowest distribution (dark blue) corresponds with the largest CCF maximums (0.80 – 0.90) while the broadest distribution (bright violet) corresponds to the set of vectors having low CCF maximums (0.1 – 0.2). Note that the sample size of each distribution is printed on the figure and varies substantially.

Figure 13: Same data as shown in Fig. 12 except as contour plots. Left: u-component differences ($U_{lidar} - \overline{U}_{sonic}$). Right: v-component differences ($V_{lidar} - \overline{V}_{sonic}$). Both as a function of the max amplitude of the CCF peak. A 3-point smooth was applied to each curve to reduce noise. The distributions become narrow as the peak amplitude of the CCF maximum increases.
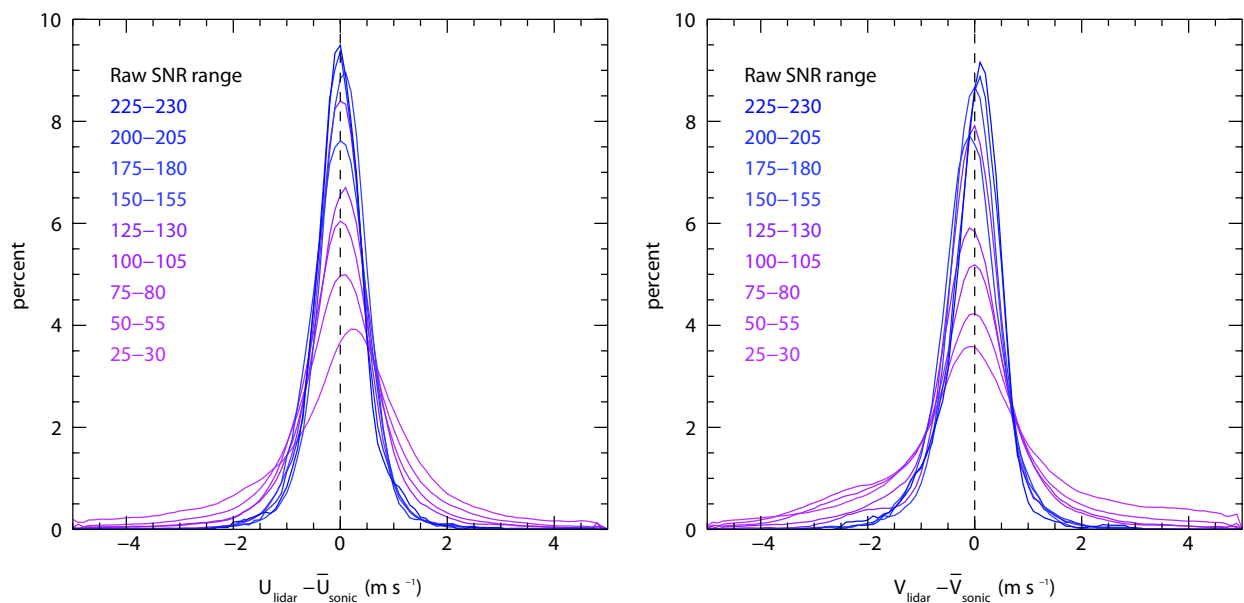
Figure 14: Distributions of the velocity component differences as a function of the mean raw SNR in the blocks used to compute the vectors. In this case, each curve corresponds to a different range of SNRs. The narrowest distributions (dark blue) correspond to high SNRs (> 150) while the broadest distribution (bright violet) corresponds to the set of vectors having low SNRs (25 - 30).
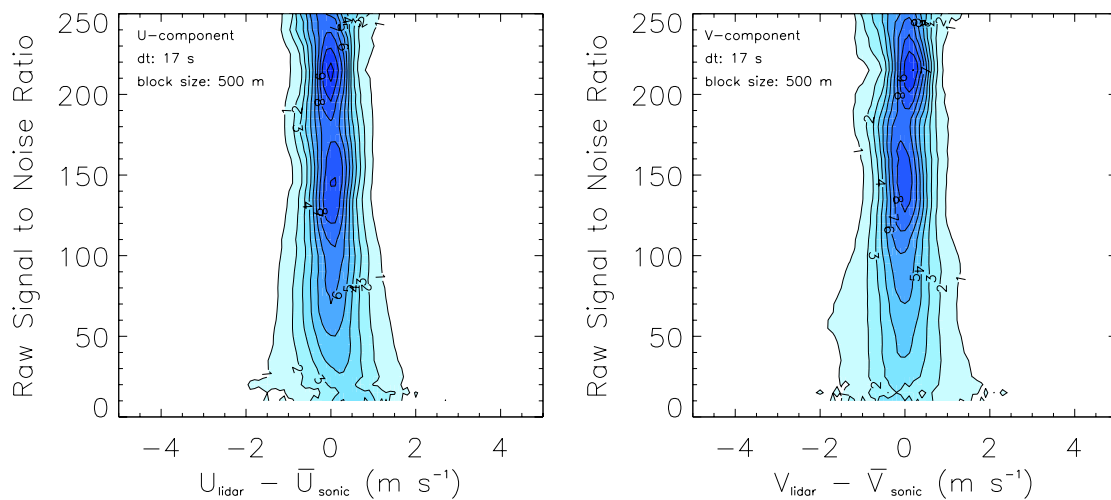

Figure 15: Same data as shown in Fig. 14 except as contour plots. Left: u-component differences ($U_{lidar} - \overline{U}_{sonic}$). Right: v-component differences ($V_{lidar} - \overline{V}_{sonic}$). Both as a function of raw SNR. A 7-point smooth was applied to each curve to reduce noise. The distributions narrow with increasing raw SNR.

tial and final positions of the aerosol perturbations in the block. As an illustration, consider two separate aerosol clouds moving in opposite directions within the same block. The resulting vector for the entire block is not the average of the two vectors representing each cloud. The CCF in this case will contain two maxima and the algorithm, as currently implemented, will select the CCF maximum that is largest. In the highly unlikely scenario that two or more maximums are identical, the first occurrence in the array containing the peaks and their locations will be selected.

This paper has described the experiment, algorithm, and preliminary data analysis results that are aimed at clarifying the accuracy and reliability of the basic cross-correlation technique when applied to aerosol lidar data. Enhancements to the basic technique may yield improved results. For example, we are currently investigating the use of recursive local-correlation (Hart, 2000) to increase the accuracy of local displacement. Recursive local-correlation is a method where a cross-correlation is performed on a region followed by another cross-correlation on the same region using a smaller block size; the larger correlation is used to limit the search for the peak in the correlation of the smaller area. Future research will include an investigation of the image SNR, the gradient Richardson number, improved gridding methods, implementation of a polynomial fit to the CCF peak, and a search for the reason causing the superior performance of the u-component.

REFERENCES

Eloranta, E. W., J. M. King, and J. A. Weinman, 1975: The determination of wind speeds in the boundary layer by monostatic lidar, *J. Appl. Meteor.*, **14**, 1485–1489.

Hart, D. P., 2000: Super-resolution PIV by recursive local-correlation, *J. Vis.*, **3**, 187–194.

Hooper, W. P. and E. W. Eloranta, 1986: Lidar measurements of wind in the planetary boundary layer: the method, accuracy and results from joint measurements with radiosonde and kytoon, *J. Clim. Appl. Meteor.*, **25**, 990–1001.

Kolev, I., O. Parvanov, and B. Kaprielov, 1988: Lidar determination of winds by aerosol inhomogeneities: motion velocity in the planetary boundary layer, *Appl. Optics*, **27**, 2524–2531.

Kunkel, K. E., E. W. Eloranta, and J. Weinman, 1980: Remote determination of winds, turbulence spectra and energy dissipation rates in the boundary layer from lidar measurements, *J. Atmos. Sci.*, **37**, 978–985.

Leese, J. A., C. S. Novak, and B. B. Clark, 1971: An automated technique for obtaining cloud motion from geosynchronous satellite data using cross correlation, *J. Appl. Meteor.*, **10**, 118–132.

Mayor, S. D., 2008: Raman-shifted Eye-safe Aerosol Lidar (REAL) observations at the Canopy Horizontal Array Turbulence Study (CHATS), in *18th Symposium on Boundary Layers and Turbulence*, AMS.

—, 2011: Observations of seven density current fronts in Dixon, California, *Mon. Wea. Rev.*, In Press.

Mayor, S. D. and E. W. Eloranta, 2001: Two-dimensional vector wind fields from volume imaging lidar data, *J. Appl. Meteor.*, **40**, 1331–1346.

Mayor, S. D., S. M. Spuler, B. M. Morley, and E. Loew, 2007: Polarization lidar at 1.54-microns and observations of plumes from aerosol generators, *Opt. Eng.*, **46**, DOI: 10.1117/12.781902.

Mayor, S. D., G. J. Tripoli, and E. W. Eloranta, 2003: Evaluating large-eddy simulations using volume imaging lidar, *Mon. Wea. Rev.*, **131**, 1428–1452.

Patton, E. G., T. W. Horst, P. P. Sullivan, D. H. Lenschow, S. P. Oncley, W. O. J. Brown, S. P. Burns, A. B. Guenther, A. Held, T. Karl, S. D. Mayor, L. V. Rizzo, S. M. Spuler, J. Sun, A. A. Turnipseed, E. J. Allwine, S. L. Edburg, B. K. Lamb, R. Avissar, R. Calhoun, J. Kleissl, W. J. Massman, K. T. P. U, and J. C. Weil, 2011: The Canopy Horizontal Array Turbulence Study (CHATS), *Bull. Amer. Meteor. Soc.*, In Press.

Piironen, A. K. and E. W. Eloranta, 1995: Accuracy analysis of wind profiles calculated from volume imaging lidar data, *J. Geophys. Res*, **100**, 25559–25567.

Rinehart, R. E. and E. T. Garvey, 1978: Three-dimensional storm motion detection by conventional weather radar, *Nature*, **273**, 287–289.

Sasano, Y., H. Hirohara, T. Yamasaki, H. Shimizu, N. Takeuchi, and T. Kawamura, 1982: Horizontal wind vector determination from the displacement of aerosol distribution patterns observed by a scanning lidar, *J. Appl. Meteor.*, **21**, 1516–1523.
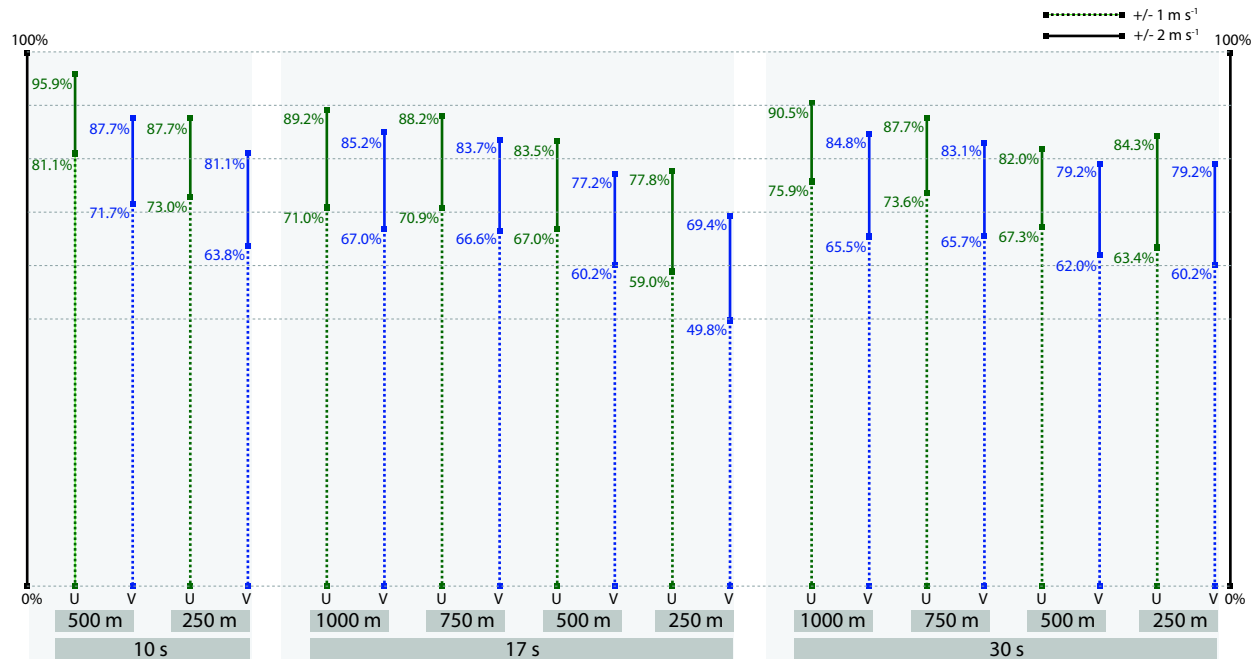
Figure 16: Summary of agreement for two components (u and v), three scan update times (10, 17, and 30 s), and four block sizes (250, 500, 750, and 1000 m). The lower of the two numbers on each bar corresponds to the percentage of comparisons that fell within $\pm\,1$ m s^{-1} of each other. The upper number corresponds to the percentage of comparisons that fell within $\pm\,2$ m s^{-1} of each other.

Schols, J. L. and E. W. Eloranta, 1992: The calculation of area-averaged vertical profiles of the horizontal wind velocity from volume imaging lidar data, *J. Geophys. Res*, **97**, 18395–18407.

Sroga, J. T., E. W. Eloranta, and T. Barber, 1980: Lidar measurements of wind velocity profiles in the boundary layer, *J. Appl. Meteor.*, **19**, 598–605.